Earth and Planetary Science Letters 401 (2014) 337–346

Contents lists available at ScienceDirect

Earth and Planetary Science Letters

www.elsevier.com/locate/epsl

Seismically deduced thermodynamics phase diagrams for the mantle transition zone

B. Tauzin *, Y. Ricard

Laboratoire de Géologie de Lyon, Terre, Planètes, Environnement, Université de Lyon, Ecole Normale Supérieure de Lyon, CNRS UMR 5276, 2 rue Raphael Dubois, 69622 Villeurbanne Cedex, France

ARTICLE INFO

Article history:
Received 13 December 2013
Received in revised form 21 May 2014
Accepted 22 May 2014
Available online 9 July 2014
Editor: P. Shearer

Keywords:
seismic discontinuities
receiver functions
mantle transition zone
phase transitions
Clapeyron slopes

ABSTRACT

Seismic discontinuities at 410 and 660 km depth are usually attributed to solid phase changes within the olivine component of the mantle. The Clapeyron slopes γ_{410} and γ_{660}, *i.e.* the thermal dependence of the depths of reactions, have been shown experimentally to be of opposite signs. Yet, their values are not well constrained by laboratory measurements. Seismological observations have not been more precise due to the difficulty to separate the competing effects of background wave-velocities and of temperature on the topography of discontinuities. In this study we use conversion imaging of interfaces under western US. We propose a new approach to derive a seismological estimate of the Clapeyron slopes with respect to γ_{410} for the major and minor phase changes of the transition zone. We obtain $\gamma_{660} \approx -3$ MPa K^{-1} for $\gamma_{410} \approx +3$ MPa K^{-1}. We construct "seismic phase diagrams" of the transition zone that can be directly compared with experimental phase diagrams. We also apply a "Z–Γ" transform to better constrain the Clapeyron slopes γ of the minor phase changes. Although tenuous, signals in seismic phase diagrams suggest that minor phase transitions, both in the olivine and the non-olivine component of the mantle, have visible seismic expressions. They can tentatively be described as follows. The '410' is overlaid at low temperature by an interface corresponding to a decrease of velocity with depth and $\gamma \approx +3$ MPa K^{-1}. The '660' widens at high temperature and is preceded at low temperature by an interface, the '620', with $\gamma \approx +7$ MPa K^{-1}. A '520' is suggested with $\gamma \approx 2$–3 MPa K^{-1}. These last two interfaces correspond to velocity increases with depth. At last, near 590 km depth, an interface may be associated with a velocity reduction showing a weak dependence on temperature ($\gamma \sim 0$ MPa K^{-1}).

1. Introduction

In the mantle, two sharp seismic discontinuities bounding the transition zone (TZ) are usually attributed to pressure-induced solid phase changes of the olivine $(Mg,Fe)_2SiO_4$ mineral. These reactions involve the transitions from olivine to wadsleyite (ol $\rightarrow$ wd) at 410 km depth (the '410'), and ringwoodite to perovskite + ferropericlase (rw $\rightarrow$ pv + fp) at 660 km depth (the '660'). Seismological observations of the depths of discontinuities can be used to probe the mantle pressure–temperature (P, T) conditions. This requires the knowledge of their Clapeyron slopes $\gamma = dP/dT$, *i.e.* the thermal dependence of the pressure at which the phase changes occur.

Laboratory experiments agree on the opposite signs of the two Clapeyron slopes. The slope γ_4 of the ol $\rightarrow$ wd transformation at 410 km depth has been measured in a $+1.5$ to $+4$ MPa K^{-1} range (Akaogi et al., 1989; Katsura et al., 2004; see Supplement Table S.1). Reports of γ_6 for the endothermic rw $\rightarrow$ pv + fp reaction at 660 km depth are even more scattered with values ranging from -4 MPa K^{-1} to -0.2 MPa K^{-1} (Ito et al., 1990; Litasov et al., 2005b). The reaction at 410 km depth should occur at higher pressure (*i.e.*, greater depth) in a hotter mantle while the '660' should occur at lower pressure (*i.e.*, lower depth) under the same condition, leading to anti-correlated topographies.

A long standing debate exists among seismologists on the degree of anti-correlation of the topographies of the '410' and '660' discontinuities. The main source of information comes from converted/reflected body-wave imaging (see Shearer, 2000, for a review). The topography of the '410' has been observed smaller than that of the '660' (Shearer, 1991; Helffrich, 2000). The unique seismological study to provide direct constraints on olivine Clapeyron slopes (Lebedev et al., 2002) found $\gamma_4 = +2$ MPa K^{-1} and $\gamma_6 = -3.3$ MPa K^{-1} below east Asia and Australia. In some cases, seismological observations are even in disagreement with the experimental expectation of anti-correlated topographies for the '410' and the '660' discontinuities. Gu et al. (1998) and

* Corresponding author.
E-mail address: benoit.tauzin@univ-lyon1.fr (B. Tauzin).

http://dx.doi.org/10.1016/j.epsl.2014.05.039
0012-821X/

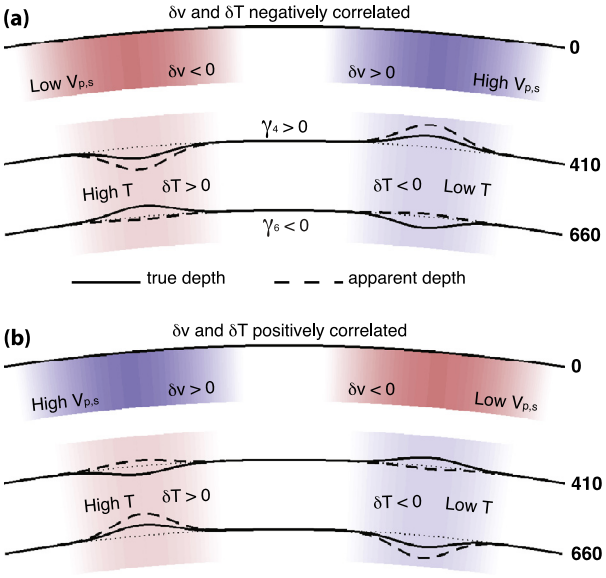

Fig. 1. Behavior of discontinuities with thermal anomalies in the transition zone and strong velocity heterogeneities in the lithosphere. Topographies of opposite signs expected from mineral physics are shown with plain lines whereas seismological observations, influenced by the uppermost velocity structure, are shown with dashed lines. In the absence of shallow corrections, an apparent correlation between the interface topographies may be observed. (a) Case of a slower lithosphere on top of a hotter mantle (left) and reciprocally (right). (b) Case of a faster lithosphere (*e.g.* due to a thin crust) on top of a hotter mantle (left) and reciprocally (right).

Houser et al. (2008) found a slight positive global correlation between them. This observation is further evidenced below hotspots (Deuss, 2007; Tauzin et al., 2008) or in the Pacific (Houser and Quentin, 2010) where the apparent $\gamma_4/\gamma_6 > 0$ has been attributed to a transition in the non-olivine component of the mantle, from majorite-garnet to perovskite in $MgSiO_3$, occurring below the '660' with a positive Clapeyron slope (Hirose, 2002).

However uncertainty remains on the reliability of the corrections for uppermost velocity structure. Interface mapping relies on the analysis of travel-times of body waves converted or reflected at discontinuities. These travel-times not only depend on the depth of conversion/reflection but also on the velocity heterogeneities encountered along the ray paths above the discontinuities. This results in a trade-off between the apparent depths of discontinuities and the velocity heterogeneities above the TZ. As depicted in Fig. 1a, shallow velocity anomalies negatively correlated with the temperature in the transition zone apparently enhance the '410' topography and reduce the '660' topography (*e.g.* the case of a hot lithosphere on top of a hot mantle, Fig. 1a, left, or reciprocally, right). Shallow velocity anomalies positively correlated with the temperature in the transition zone could lead to an overestimate of the '660' topography compared to that of the '410' (*e.g.* a thin crust on top of a hotter mantle, Fig. 1b, left, or reciprocally, right). In general, the absence or the inaccuracy of velocity corrections obscure the anti-correlation between the discontinuity depths (*e.g.* Stammler and Kind, 1992). In extreme cases where the contribution from shallow velocity heterogeneities exceeds the contribution from the temperature (*i.e.*, all 4 cases in Fig. 1), the topographies appear correlated and the apparent Clapeyron slope ratio γ_4/γ_6 becomes positive, contrary to experimental expectations. This could be especially the case for up-going P waves converted into shear waves under seismological stations (P-to-S conversions) whose travel-times are strongly velocity-dependent (Li et al., 2003).

In this study, we propose a method to separate the competing effects of uppermost velocity structure and temperature on the topography of TZ discontinuities. This method makes possible the determination of the ratio γ_4/γ_6 with little information on the background velocity structure. From this estimate, we can correct the structure of the TZ from the effect of velocities, estimate the temperature, and build diagrams that may be used as a proxy for thermodynamics phase diagram of solid–solid transitions. Then we develop and apply a new method, the "Z–Γ stacking", to test the presence of unknown phase transitions in the mantle and measure their relative Clapeyron slopes.

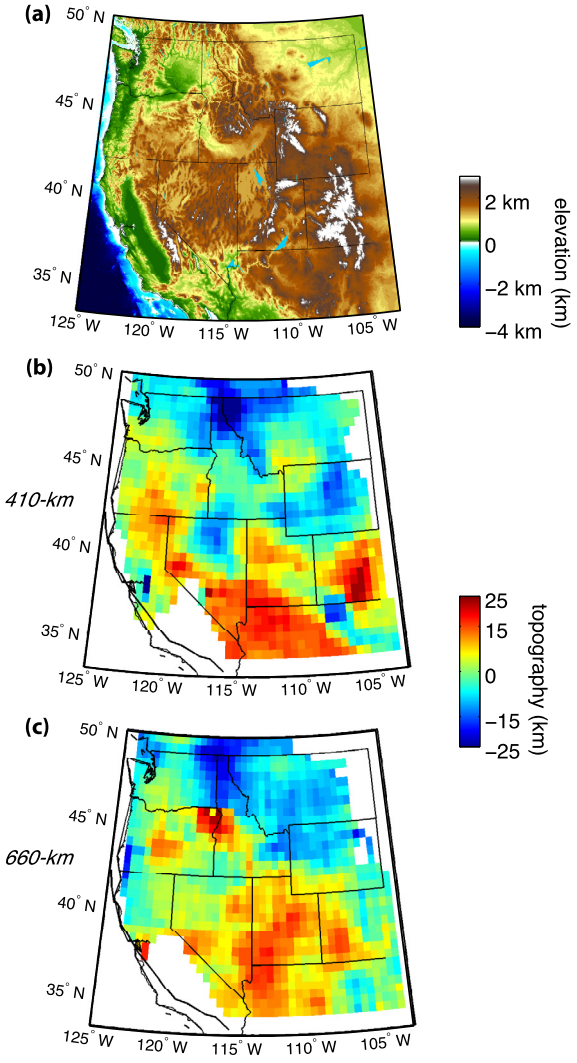

Fig. 2. (a) Surface topography with state borders. (b) Apparent topography δZ_4 of the '410' seismic discontinuity. (c) Apparent topography δZ_6 of the '660' discontinuity (both panels from Tauzin et al., 2013).

2. Seismic observations under western US

We make use of a dataset of P-to-S conversions obtained from the Transportable Array component of USArray. This dataset is described in detail in Tauzin et al. (2013). Using receiver functions, the mantle structure of the western half of the US (Fig. 2a) has been characterized in the 5–75 s period range. Seismic images of mantle discontinuities have been produced by a migration method, stacking the receiver functions by common conversion point (CCP) (Dueker and Sheehan, 1997; Wittlinger et al., 2004). The imaged volume is thus called a "CCP volume". By picking in this volume the seismic signal of conversions at the '410' and '660', high resolution maps of their apparent topographies (δZ_4 and δZ_6) have been obtained on a 0.5° grid in latitude and longitude (Fig. 2b, c). The observed average depths of the '410' and '660' over the area

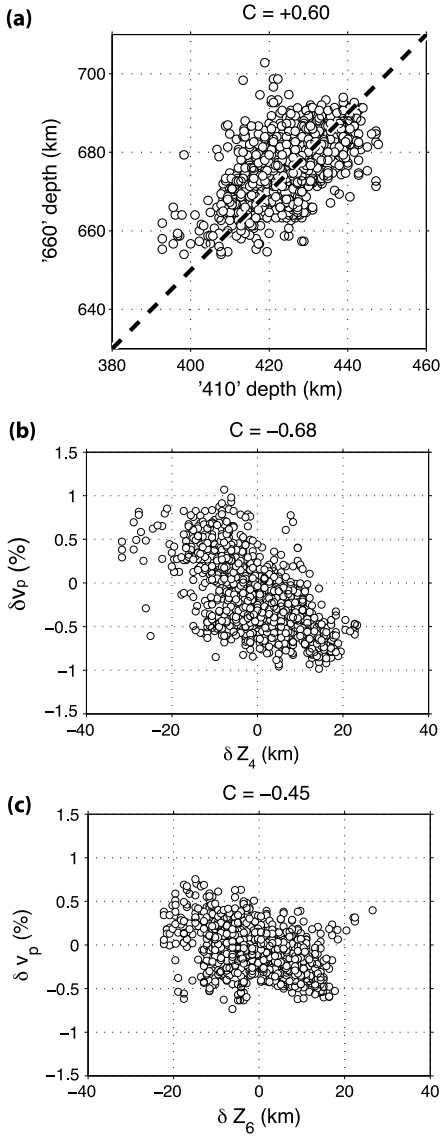

Fig. 3. (a) Observed '660' depth Z_6 versus the '410' depth Z_4. The oblique dashed line represents perfectly correlated topographies. (b) Average tomographic velocity anomalies δv_p above the '410' versus the '410' topography δZ_4. (c) Average tomographic velocity anomalies δv_p above the '660' versus the '660' topography δZ_6. The tomographic model is from Burdick et al. (2010). Correlation coefficients are indicated at the top. The two topographies appear positively correlated contrary to mineralogical expectations. Their negative correlations with the shallow velocity suggest a large effect of the shallow structure on the apparent depths of discontinuities.

are $\langle Z_4 \rangle = 424$ km and $\langle Z_6 \rangle = 676$ km. The corresponding peak-to-peak depth variations are 55 km for the '410' and 49 km for the '660' (with RMS 9.8 km and 8.8 km, respectively). The migration being performed using a spherical model, IASP91 (Kennett and Engdahl, 1991), the topography maps do not take into account lateral variations of velocities within the mantle. We thus expect shallow velocity heterogeneities to significantly affect the apparent topography of TZ discontinuities.

Fig. 3 shows that this is indeed the case. Contrary to mineral physics expectations, the '410' and the '660' topographies have a positive correlation of +0.60 (in all the paper we note $\langle x \rangle$ the average of the variable x, $\delta x = x - \langle x \rangle$ the deviation from average, and we use the Pearson's correlation coefficient between x and y defined as $\langle \delta x \cdot \delta y \rangle / \sqrt{\langle \delta x \cdot \delta x \rangle \langle \delta y \cdot \delta y \rangle}$). This correlation (Fig. 3a) is partly the result of shallow velocity heterogeneities in the mantle overlying the TZ. The depth–velocity trade-off is obvious by looking at average δv_p anomalies above the TZ taken from the tomographic model of Burdick et al. (2010), versus the '410' topography in Fig. 3b. The correlation is negative, −0.68, as a slower lithosphere tends to increase the apparent depths of the discontinuities (see Fig. 1a, left, and Fig. 1b, right). This trade-off reduces slightly to −0.45 when examining the '660' topography (Fig. 3c). Similar observations from SS-precursors have already been discussed by Houser et al. (2008).

3. Clapeyron slopes of the '410' and the '660'

3.1. Seismic imaging of discontinuities

We assume that at first order, the "depth variation" δZ of a phase transition depends on its Clapeyron slope, γ and on the temperature variations δT (*i.e.* the temperature minus the adiabatic reference geotherm). The potential effects of compositional heterogeneities (*e.g.*, water content or variability in Mg/Fe ratios, Litasov et al., 2005a; Irifune et al., 1998) are considered as second order effects. Depth and temperature are therefore related by

$$\delta Z = Z - \langle Z \rangle = \frac{\gamma}{\rho g} \delta T = \Gamma \delta T \tag{1}$$

where g is Earth's gravity, ρ the density above the discontinuity and Γ the Clapeyron slope in $\mathrm{m\,K^{-1}}$ (while γ is in $\mathrm{Pa\,K^{-1}}$, see Helffrich and Bina, 1994). The absolute depth of discontinuity Z and its average $\langle Z \rangle$, can be directly estimated from seismic imaging using for instance P-to-S conversions (Tauzin et al., 2013) or SS-precursors (Houser et al., 2008). In the case of our P-to-S observations, the travel times of converted waves Pds relative to the direct P depend on the conversion depth Z, the ray parameter p (assumed to be identical for the two waves), the S and P velocities v_s, v_p:

$$t_{Pds}(p, Z) = \int_0^Z \left[\sqrt{v_s^{-2} - p^2} - \sqrt{v_p^{-2} - p^2} \right] dz \tag{2}$$

Supposing v_p and v_s perfectly known, this equation enables the projection of the amplitude measured at time t_{Pds} on a seismogram at the "true" depth Z (this is called time-to-depth conversion). A more sophisticated but similar approach for interface imaging is to backpropagate the seismic wavefield recorded at the surface, with the expectation that the transposed wavefield will focus at and therefore will highlight the sources of seismic scattering in the subsurface (this is called migration; *e.g.*, Rondenay, 2009).

However in these methods, the imperfect knowledge of the shallow velocity structure leads to an imperfect recovery of the interface positions. Instead, one recovers an apparent topography:

$$\delta Z = Z - \langle Z \rangle = \Gamma \delta T + \delta h \tag{3}$$

The correction term δh integrates the effects on travel-times of 3D heterogeneities $\delta v_{s,p}$ ($\delta v = v - v_{ref}$) encountered along the ray paths and not taken into account by the reference model. Instead of (2) what is really used is:

$$t_{Pds}(p, Z) = \int_0^{Z+\delta h} \left[\sqrt{v_{s_{ref}}^{-2} - p^2} - \sqrt{v_{p_{ref}}^{-2} - p^2} \right] dz \tag{4}$$

where $v_{s_{ref}}$ and $v_{p_{ref}}$ are velocities in the Earth's reference model used for imaging. The deviations of velocities $\delta v_{s,p}$ from the reference model are thus mapped into δh. Using (2), the latter identity can be used to express δh, assuming a vertical incidence ($p = 0$):

$$\delta h = -\frac{\int_0^Z [\delta v_s / v_{s_{ref}}^2 - \delta v_p / v_{p_{ref}}^2] dz}{[1/v_{s_{ref}}(Z) - 1/v_{p_{ref}}(Z)]} \tag{5}$$

(practically, the P and S ray paths are not vertical so (5) is an approximation). In general δv_s and δv_p are correlated, and $|\delta v_s/v^2_{s_{ref}}| > |\delta v_p/v^2_{p_{ref}}|$, so that δh is anti-correlated with the seismic velocities above the TZ, *i.e.* deeper interfaces $\delta h > 0$ are inferred for a slower lithosphere $\delta v_{s,p} < 0$ (see Fig. 1 and Fig. 3b, c).

The effect of δh can in principle be estimated from tomographic imaging. However, the travel-time tomography is often resolved with longer wavelengths than what would be needed to accurately correct the local information associated with converted/reflected body waves, especially at global scale.

To alleviate the problem of mapping velocity variations into interface topographies, various authors have discussed their results in term of TZ thickness (*e.g.*, Chevrot et al., 1999; Lawrence and Shearer, 2006; Tauzin et al., 2008). Computing a difference of topographies cancels the major corrections due to the shallow structure but leaves those due to the velocity perturbations in between the two interfaces. For example, because of local temperature variations, any possible interface within the TZ, appears shifted with respect to the '410', by the distance, see (5),

$$\delta h_T(Z) = a(Z)\delta T = -K\frac{\int_{Z_4}^{Z}[1/v_{s_{ref}} - 1/(Rv_{p_{ref}})]\,dz}{[1/v_{s_{ref}}(Z) - 1/v_{p_{ref}}(Z)]}\delta T \tag{6}$$

where the proportionality factor computed at the '660' is $a(\langle Z_6\rangle) = a_6 = 0.03\ \mathrm{km\,K^{-1}}$ (using $K = \partial \log v_s/\partial T = -7\times 10^{-5}\ \mathrm{K^{-1}}$ (Stixrude and Lithgow-Bertelloni, 2005) and $R = \partial \log v_s/\partial \log v_p = 2$ (*e.g.*, Schmandt and Humphreys, 2010; Becker, 2011)). The contributions of the lateral temperature variations to the apparent thickness of the TZ are therefore non-negligible (3 km for 100 K) and a hotter TZ appears thicker without corrections.

3.2. Fundamental hypotheses

For the '410' and the '660' discontinuities, we suppose that the apparent topographies are given by:

$$\begin{aligned}\delta Z_4 &= \Gamma_4\delta T + \delta h\\ \delta Z_6 &= \Gamma_6\delta T + \delta h + \delta h_T\big(\langle Z_6\rangle\big) = (\Gamma_6 + a_6)\delta T + \delta h = \Gamma_6'\delta T + \delta h\end{aligned} \tag{7}$$

In the last equality we group together the two δT-dependent terms and define an apparent Clapeyron slope $\Gamma_6' = \Gamma_6 + a_6$. Eqs. (7) assume that the temperature δT in the TZ does not vary with depth but uniquely laterally. We will discuss this approximation in Section 3.5.

The expectation from high pressure mineral physics is that $\Gamma_6/\Gamma_4 < 0$. This effect alone imposes a negative correlation between δZ_4 and δZ_6 (see (7)). On the contrary, the contribution of δh is opposite (see (7)). As a_6 and Γ_4 have the same sign, the temperature variations within the TZ also tend to increase the correlation between the interfaces. The slight positive correlation observed between the '410' and '660' topographies at a global scale (Gu et al., 1998; Houser et al., 2008) could thus be partly explained by an under-estimation of the velocity corrections.

3.3. The Clapeyron slope ratio and temperature in the TZ

Writing $\Gamma_4\delta Z_6 - \Gamma_6'\delta Z_4$ (see (7)), we get the contribution from the shallow heterogeneities as a function of an apparent Clapeyron slope ratio (Γ_6'/Γ_4)

$$\delta h = \frac{1}{1-\Gamma_6'/\Gamma_4}\delta Z_6 - \frac{1}{\Gamma_4/\Gamma_6' - 1}\delta Z_4 \tag{8}$$

Our method considers the contribution δh as a noise to the real signal, that must be minimized, *i.e.*, we choose the Clapeyron ratio Γ_6'/Γ_4 that explains the ensemble of observations in terms of temperature variations and shallow corrections, but requires the smallest shallow corrections. We therefore look for the ratio Γ_6'/Γ_4 that minimizes the quantity:

$$\chi^2 = \langle \delta h^2\rangle \tag{9}$$

We can show that an analytical solution to $\partial\chi/\partial(\Gamma_6'/\Gamma_4) = 0$ is:

$$\frac{\Gamma_6'}{\Gamma_4} = \frac{\langle \delta Z_6\cdot(\delta Z_6 - \delta Z_4)\rangle}{\langle \delta Z_4\cdot(\delta Z_6 - \delta Z_4)\rangle} \tag{10}$$

The expression (10) can also be understood from a different standpoint. The shallow corrections and the temperature in the transition zone are likely uncorrelated on average. The shallow corrections are mostly due to crustal anomalies and fossil structure of the lithosphere. Their correlation with the thermal TZ structure is very low in global tomography models (see *e.g.*, Becker and Boschi, 2002). We may therefore assume that the correlation between δh and δT is zero, *i.e* $\langle \delta T\cdot\delta h\rangle = 0$. We discuss further the validity of this assumption in Section 3.5. In this case, one has simply from (7)

$$\begin{aligned}\langle \delta Z_4\cdot\delta Z_4\rangle &= \Gamma_4^2\langle \delta T\cdot\delta T\rangle + \langle \delta h\cdot\delta h\rangle\\ \langle \delta Z_6\cdot\delta Z_6\rangle &= \Gamma_6'^2\langle \delta T\cdot\delta T\rangle + \langle \delta h\cdot\delta h\rangle\\ \langle \delta Z_6\cdot\delta Z_4\rangle &= \Gamma_4\Gamma_6'\langle \delta T\cdot\delta T\rangle + \langle \delta h\cdot\delta h\rangle\end{aligned} \tag{11}$$

Subtracting the last equation to the first two and removing the term $\langle \delta T\cdot\delta T\rangle$ by division, leads again to the relation (10). In conclusion, choosing the Clapeyron slope ratio according to (10) simultaneously minimizes the overall shallow corrections and their correlations with the TZ structure.

The minimization process allows us to compute the ratio of the apparent Clapeyron slopes, Γ_6'/Γ_4 but not the two mineralogical Clapeyron slopes γ_6 and γ_4, independently. If one of the Clapeyron slopes is known, *e.g.* at the '410', then the Clapeyron slope of the '660' is obtained from

$$\gamma_6 = \frac{\rho_6}{\rho_4}\frac{\Gamma_6'}{\Gamma_4}\gamma_4 - \rho_6 g a_6 \tag{12}$$

where ρ_4 and ρ_6 are the reference densities above the '410' and '660'.

From $\delta Z_4 - \delta Z_6$ (see (7)), we obtain the TZ temperature as:

$$\delta T = \frac{1}{\Gamma_4}\frac{1}{(1-\Gamma_6'/\Gamma_4)}(\delta Z_4 - \delta Z_6) \tag{13}$$

The temperature field within the TZ is thus linearly related to the variations in TZ thickness. The thermal contributions to the '410' topography, *i.e.*, $\Gamma_4\delta T$, are obtained by our method but we must assume the independent knowledge of one of the Clapeyron slopes (*e.g.* Γ_4) to obtain δT.

3.4. Application to western US

In the following, we use our observations of apparent topographies of TZ discontinuities below western US to estimate the ratio of the '410' and '660' Clapeyron slopes. We plot in Fig. 4 the root mean square function $\chi(\Gamma_6'/\Gamma_4)$ (9) which goes through a minimum at $(\Gamma_6'/\Gamma_4) = -0.56$, given, as expected, by (10). We find no minima for positive values of (Γ_6'/Γ_4). According to (12), we therefore predict a relation between the mineralogical Clapeyron slopes

$$\gamma_6 = -0.64\gamma_4 - 1.17 \tag{14}$$

where we used $a_6 = 0.030\ \mathrm{km\,K^{-1}}$, $\rho_4 = 3542\ \mathrm{kg\,m^{-3}}$, and $\rho_6 = 3991\ \mathrm{kg\,m^{-3}}$. For $\gamma_4 = +3.0\ \mathrm{MPa\,K^{-1}}$, we obtain $\gamma_6 = -3.1\ \mathrm{MPa\,K^{-1}}$ and $\gamma_4/\gamma_6 = -1.03$.

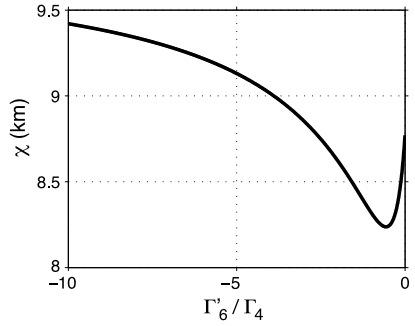

Fig. 4. The minimization of the shallow corrections (see (9)) occurs for $\Gamma_6'/\Gamma_4 = -0.56$.

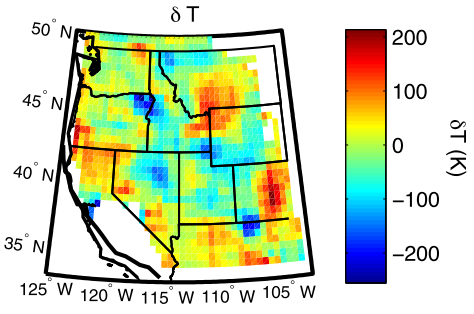

Fig. 5. Map of temperature anomalies δT within the TZ obtained from (13) and $\gamma_4 = +3.0$ MPa K^{-1}.

We show in Fig. 5 the result of applying (13) with $\Gamma_6'/\Gamma_4 = -0.56$ and taking $\gamma_4 = +3.0$ MPa K^{-1}, close to the average of experimental values in Table S.1. As expected from Eq. (13), the pattern of thermal anomalies is proportional to the TZ thickness (Tauzin et al., 2013). The choice of γ_4 determines the range of thermal variations δT, from −259 K below northeast Oregon to +216 K below Yellowstone, with a 65 K RMS (Fig. 5). This temperature is weakly but positively correlated with what can be estimated from tomography in the TZ (correlation of +0.23 with Burdick et al., 2010's model at mid TZ). The average horizontal temperature gradient is of order 0.7 K km^{-1}, comparable to the adiabatic gradient in the transition zone (Katsura et al., 2010).

In Fig. 6a, we plot a map of the depth corrections δh computed from (8) and $\Gamma_6'/\Gamma_4 = -0.56$. These corrections should represent the contribution of shallow velocity heterogeneities to the interface topographies. A clear NE–SW dichotomy is observed with δh values ranging from −25 km below northern Idaho to +17 km in the southwest of Utah, with an RMS of 8.5 km. This dichotomy dominates the initial maps of topographies (Fig. 2b, c).

The corrections δh can be compared with those, δh_{tomo} computed with the P-wave model of Burdick et al. (2010) (Fig. 6b). To estimate δh_{tomo}, a shear-wave model δv_s is required (5). We scale δv_s from δv_p using $\delta \log v_s / \delta \log v_p = 2$ (*e.g.*, Romanowicz and Cara, 1980; Schmandt and Humphreys, 2010). This value of $\delta \log v_s / \delta \log v_p$ has no impact on the high correlation between δh and δh_{tomo}, +0.65. The amplitudes of δh_{tomo} are generally lower than predicted with our method (Fig. 6a) but the NE–SW dichotomy is well recovered. This confirms the dominant effect of shallow velocities on the apparent topographies of TZ discontinuities.

The corrections δh and $\delta h + a_6 \delta T$ must be removed from the observed topographies δZ_4 and δZ_6 to obtain the "true" topographies (7), perfectly anti-correlated by construction and due to temperature variations alone (Fig. 6c and d). The estimated Clapeyron slope ratio γ_6/γ_4 being ∼−1.0, the relative amplitudes of thermal topographies are similar. In term of RMS amplitudes the initial topographies for the '410' and '660' are of 9.8 and 8.8 km, from which we removed a shallow correction related to δh of 8.5 km, a temperature correction at '660' related to $a_6 \delta T$ of 1.9 km, leaving thermal topographies of 5.3 and 4.9 km respectively.

3.5. Critical assessment

Our method makes use of two hypotheses: a low correlation between the shallow corrections and the temperature in the TZ and a TZ temperature varying only laterally. These hypotheses allow us to correct the direct observations of interface topographies without using a tomographic model.

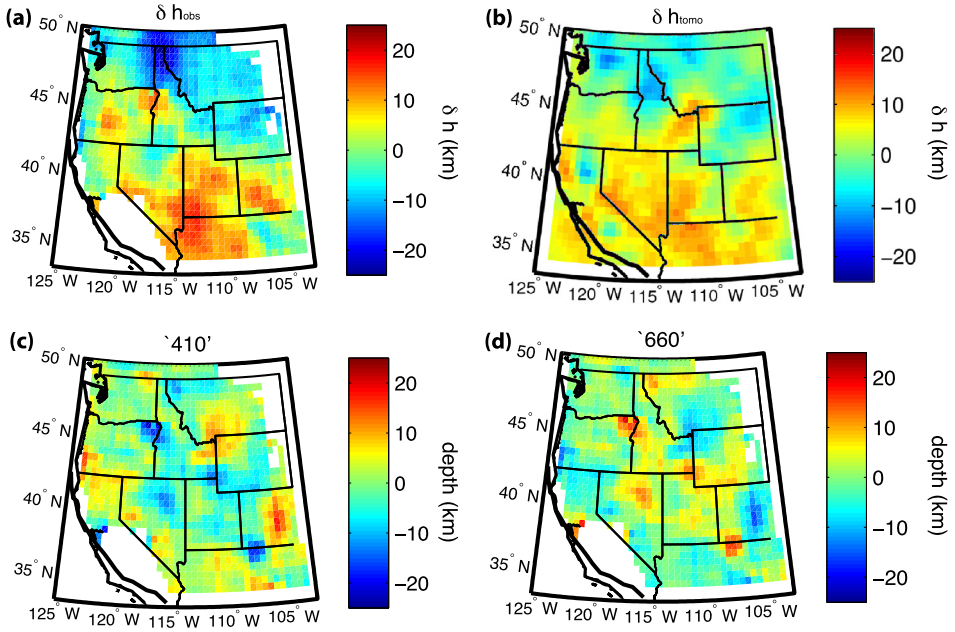

Fig. 6. (a) Map of the depth corrections δh obtained with the apparent Clapeyron slope ratio $(\Gamma_6'/\Gamma_4) = -0.56$. (b) Map of the corrections δh_{tomo} (5) computed with the δv_p model of Burdick et al. (2010) and $R = \partial \ln v_p / \partial \ln v_s = 2$. (c) Map of the '410' thermal topography $\Gamma_4 \delta T$. (d) Map of the '660' thermal topography $\Gamma_6 \delta T$. The thermal topographies have been computed with $\gamma_4 = +3.0$ MPa K^{-1}.

Our assumption of a weak correlation between the shallow correction and the temperature in the TZ is in relative agreement with Burdick et al. (2010)'s model where the shallowest 400 km (a proxy for shallow corrections) are weakly correlated (-0.17) with the tomographic anomalies at 500 km (a proxy for the TZ structure). In Supplement S.1, we discuss how this correlation $C(\delta h, \delta T)$ may affect our results. When $C(\delta h, \delta T)$ varies from -0.2 to $+0.2$, we show that the ratio Γ_6'/Γ_4 derived from the data changes from -0.19 to -1.23. The assumption of an uncorrelation between shallow corrections and the TZ temperature is therefore crucial. Using the correlation value suggested by Burdick's mantle model would change our estimate for Γ_6'/Γ_4 from -0.56 to -0.23, or using (14), our estimate of γ_6 from -3.1 to -2.0 MPa K^{-1}. Note that crustal heterogeneities, which are not explicitly given in the mantle model of Burdick et al. (2010) should rather decrease than increase $|C(\delta h, \delta T)|$. With $C(\delta h, \delta T) = -0.17$ the RMS thermal topography at '410' slightly increases from 5.3 to 6.2 km, that at '660' decreases from 4.9 to 4.3 km, and the RMS of the corrections δh does not change much with $C(\delta h, \delta T)$.

In Supplement S.2, we also discuss the assumption of a uniform temperature in the TZ. We show that as soon as the RMS of the difference of temperature between the two interfaces is lower than that of the lateral variations, the retrieved Γ_6'/Γ_4 is not significantly affected. The fact that the vertical difference of temperature in the 250 km thick TZ (corrected from the adiabatic gradient) is not larger than the horizontal temperature differences below western US seems reasonable.

Therefore, the accuracy of our method is mostly affected by the assumption of an uncorrelation between surface corrections and the TZ temperature and not much by the sampling of our dataset (we checked by bootstrap resampling that similar results are obtained by using only subsets of our data) or by the assumption of a vertically uniform TZ. Of course, if tomographic models were extremely precise they could be used to correct the observations or to check our hypotheses. Unfortunately, we consider that this appears difficult even with high quality models like that of Burdick et al. (2010).

First, tomographic inversions involve smoothing and regularization that limit their accuracy at the short length-scale at which interface topographies are mapped by receiver functions. Even under the well-mapped upper mantle below western US, the resolution is at least 200 km (Becker, 2011). Second, velocity variations close to an interface, can be interpreted as due to temperature variations in a medium with flat interfaces or as due to interface undulations in a medium without other velocity anomalies. In the first case we would assume that $\delta v_p/v_p = (\partial \log v_p/\partial T)\delta T \approx -3.5 \times 10^{-5}\delta T$. In the second case, an interface topography $\delta Z = \Gamma \delta T$ seen with a vertical resolution λ would appear as an anomaly $\delta v_p/v_p = -(\Delta v_p/v_p)(\Gamma/\lambda)\delta T$ where $\Delta v_p/v_p$ is the velocity jump across the interface ($\Delta v_p/v_p \approx 4\%$ and 6% at the '410' and '660'). We would obtain $\delta v_p/v_p \approx -10^{-5}\delta T$ near the '410' and $\delta v_p/v_p \approx +4 \times 10^{-5}\delta T$ near the '660' for a resolution length of $\lambda = 100$ km. Of course a combination of the two effects is likely. The above numerical applications imply that we may not even know the sign of the temperature anomaly near the '660' and that accurate temperature estimate at '410' is unlikely. It seems to us that unless tomographic models are obtained by simultaneous inversion of both velocities and interfaces (like *e.g.* in Gu et al., 2003; Houser et al., 2008; Lawrence and Shearer, 2008, but with a better regional resolution), the estimate of TZ temperatures from tomographic models with flat interfaces will introduce more, or at least as much uncertainties as our simpler approach.

4. Phase changes in the transition zone

4.1. Seismically deduced phase diagrams

Now that we have estimated the velocity corrections and the TZ temperature we can directly use the waveforms to construct a representation of the thermodynamic phase diagram seen from seismology and to search for other potential phase changes.

In Fig. 7a, we stack all the seismic signals $s_i(Z)$ within intervals of apparent depths δZ_4 of the '410'. The '410' and the '660' appear as well-resolved streaks. The slopes of δZ_4 and δZ_6, both positive in this diagram, are controlled by shallow heterogeneities δh (see (7)). Their slight difference is due to the weak expression of temperature.

A more meaningful observation of the interfaces is obtained by correcting the traces from the shallow heterogeneities, hence by considering $s_i(Z - \delta h_i)$ where δh_i is given by (8) and (10). This is done in Fig. 7b, here as a function of the thermal topography of the '410', $\Gamma_4 \delta T$. The effect of the corrections is drastic on the '660', straightening it up to an opposite direction to that of the '410'.

All the interfaces in the TZ are also displaced by $a(Z)\delta T$ (see (6)). The best representation of the effects of the temperature on phase changes is obtained by plotting the function $F(Z, \delta T)$ (see Fig. 7c) obtained by stacking $s_i(Z - h_i - a(Z)\delta T_i)$ as a function of δT_i

$$F(Z, \delta T) = \left\langle s_i\left(Z - h_i - a(Z)\delta T_i, \delta T_i\right)\right\rangle \quad \text{for } \delta T_i \approx \delta T. \tag{15}$$

The function $F(Z, \delta T)$ represents our best estimate of the position of the interfaces as a function of temperature, what we call a "seismic phase diagram". Note that the construction of this diagram requires the choice of the '410' Clapeyron slope to properly scale δT. Here we choose $\gamma_4 = +3.0$ MPa K^{-1}. In this "seismic phase diagram" the phase changes at '410' and '660' are straight lines with slopes Γ_4 and Γ_6. Any other phase transformation appears as a line of slope Γ. The ol $\rightarrow$ wd and rw $\rightarrow$ fp + pv are clearly visible but the wd $\rightarrow$ rw transition is very faint (encircled by a dashed ellipse in Fig. 7d). Other signals in the diagram can either be associated with phase transitions if they align on linear trends, or with "noise" if they do not, due for instance to compositional effects.

This approach can also be used to correct seismic sections for the mantle (see Fig. S.2). As an example, the initial section for a profile at 41°N is corrected from the shallow heterogeneity and the temperature induced velocity changes and leads to a profile where the signal should be only due to the true interface undulations.

Tauzin et al. (2013) reported the presence of seismic discontinuities around 350, 590 and 620 km depths in the mantle below western US. These features are more local than the '410' and '660' but appear anyway in the diagram of Fig. 7c. For cold regions of the mantle (<-150 K of thermal anomaly), a negative signal is observed atop the '410' around 380 km depth (the '350'). This same temperature domain is characterized by multiple positive peaks above the '660' and by what we can associate with a positive '620' discontinuity. The negative signal of the '590' is diffuse: it can be found across the whole temperature range with higher amplitudes in the hottest environments (dotted contour in Fig. 7d). We checked by making seismic phase diagrams restricted to the eastern or western regions relative to the Nevada/Utah borders, that the characteristics of our observations in Tauzin et al. (2013) are preserved. We observe the '350' in both eastern and western regions with stronger amplitudes in the west, the negative '590' mostly in the east, and the positive '620' in both areas. This confirms that these minor interfaces are robust in their seismological observation.

The minor interfaces seem also consistent with our model of phase changes and vertically coherent temperature in the TZ. They

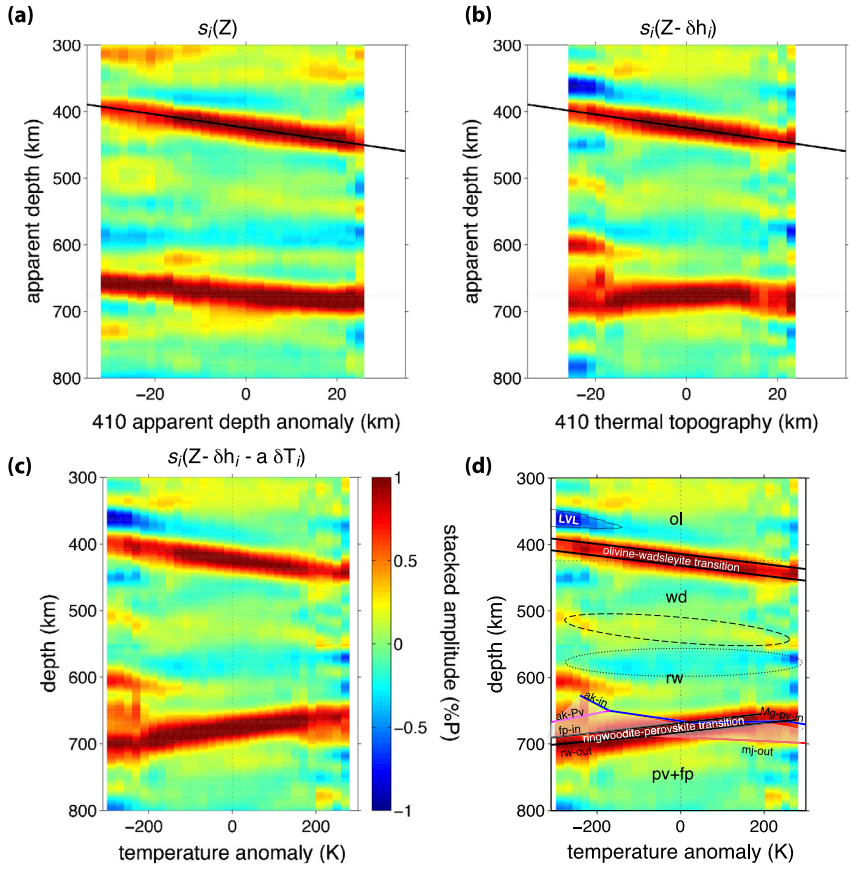

Fig. 7. (a) Diagram of the seismic signals $s_i(Z)$ stacked within 2 km intervals of the apparent depth of the '410', δZ_4. Positive amplitudes (in red) mark velocity increases with depth whereas negative amplitudes (in blue) are associated with velocity reductions. The black line is the relation $Z = \langle Z_4 \rangle + \delta Z_4$. (b) Diagram of $s_i(Z - \delta h_i)$, corrected from shallow heterogeneities. The black line is the relation $Z = \langle Z_4 \rangle + \delta Z_4 - \delta h = \langle Z_4 \rangle + \Gamma_4 \delta T$. (c) Seismic phase diagram $F(Z, \delta T)$ (using $\gamma_4 = +3$ MPa K^{-1} and stacking the seismic signal by intervals of 20 K). (d) Our interpretation. ol: olivine; wd: wadsleyite; rw: ringwoodite; fp: ferropericlase; pv: perovskite; mj: majorite; ak: akimotoite. LVL: Low velocity layer atop the '410'. The phase diagram for transformations at the bottom of the transition zone is taken from Hirose (2002) for pyrolite. The dashed ellipse locates the weak signal from a possible wd → rw transition and the dotted ellipse the signal of the negative '590'. (For interpretation of the references to color in this figure legend, the reader is referred to the web version of this article.)

are not noise or random scatterers because they are seen coherently in quite specific domains of temperature in the diagram. Indeed, they do not appear as coherent as we stack the data as a function of the apparent '410' topography (see Fig. 7a). Their origin is thus likely related to the temperature in the TZ.

4.2. Z–Γ stacking for the Clapeyron slope of unknown phase transitions

This seismic phase diagram suggests a simple way to interrogate the data for the presence of phase transitions in the mantle. We simply stack all the observations, corrected from the velocity perturbations, along the lines of slopes Γ. This method is akin to the slant stack τ–p method (Rost and Thomas, 2002) or the more general Radon transform (Gu and Sacchi, 2009) that sum up signals, not at constant depth (or time) but along a specific integration path. We thus build a Z–Γ diagram $G(Z, \Gamma)$,

$$G(Z, \Gamma) = \int F(Z - \Gamma \delta T, \delta T)\, \mathrm{d}T \tag{16}$$

This function (see Fig. 8) presents two maxima at $Z = 424$ km and $\Gamma = +0.081$ km K^{-1} for the '410' and at $Z = 677$ km and $\Gamma = -0.079$ km K^{-1} for the '660'. Their Clapeyron slope ratio is close to the estimate of Section 3.4 (here we compute the maximum of an average signal while in Section 3.4 we compute the average of the positions of maxima: this explains the small difference). As reported in Tauzin et al. (2013) the amplitudes of the signals converted at the '410' and '660' are comparable (∼1% of the P signal) while radial models (PREM or IASP91) would predict a 50% larger signal for the conversion at the '660' which suggests that radial models overestimate the velocity jump at the '660'. It is possible that IASP91 maps into a single sharp velocity jump what is actually a more gradual velocity increase (Schmandt, 2012). Other maxima in the $G(Z, \Gamma)$ diagram potentially indicate the presence of additional phase transitions in the mantle near the depth Z and with a Clapeyron slope Γ.

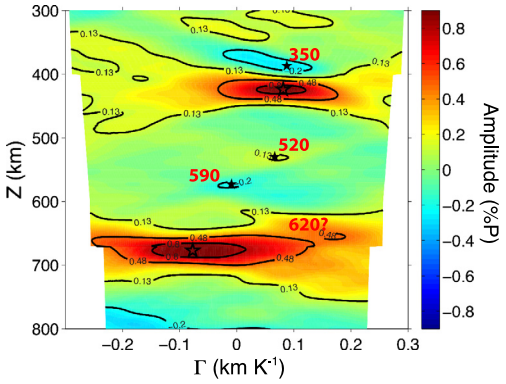

Fig. 8. Z–Γ diagram. The amplitudes are red (positive) for velocity increases and blue (negative) for velocity reductions. The stars correspond to the couples $(\langle Z \rangle, \Gamma)$ expected for the '410' and '660' and inferred for minor extrema that are found around 350, 520, 590 and 620 km depths. (For interpretation of the references to color in this figure legend, the reader is referred to the web version of this article.)

Table 1
Summary of potential phase transitions observed in the TZ.

Discontinuity	Γ (km K^{-1})	γ (MPa K^{-1})	Depth (km)	Amplitude (% 410)	Possible transition	γ (MPa K^{-1})
'410'	+0.081	+2.8	424	100	ol → wd	γ_4
'660'	−0.079	−3.1	677	110	rw → pv + fp	$-0.64\gamma_4 - 1.17$
'350'	+0.092	+3.2	387	−30	LVL	$1.0\gamma_4 + 0.25$
'520'	+0.064	+2.5	530	+14	wd → rw	$1.0\gamma_4 - 0.50$
'590'	−0.010	−0.4	573	−22	?	$0.15\gamma_4 - 0.83$
'620'	+0.174	+6.8	656	+54	mj → ak	$2.59\gamma_4 - 0.98$

The additional minor seismic discontinuities reported in Tauzin et al. (2013) and in Fig. 7c are also present as weak local extrema in the Z–Γ domain (small stars). The '350' is recovered at 387 km depth with an apparent Clapeyron slope $\Gamma = +0.092$ km K^{-1} and the '590' at 573 km with $\Gamma = -0.010$ km K^{-1}. The two discontinuities have absolute amplitudes within 20 to 30% of the '410' or '660' amplitudes (*i.e.* ∼0.3% the P-wave amplitude). A peak at $Z = 530$ km and $\Gamma = +0.064$ km K^{-1} could correspond to the wd → rw transition but the signal is weak with an amplitude of only 0.1% the P-wave (*i.e.* 14% the conversion at the '660'). The '620' appearing as a conspicuous feature in Fig. 7c is not reliably constrained with our Z–Γ stacking approach because it is close to the strong signal from the '660'.

A summary of our results is given in Table 1. In the second and third columns Γ and γ assume $\gamma_4 = +3$ MPa K^{-1}. The depths reported in the fourth column correspond to the potential depth of the interface in a reference mantle with zero thermal anomalies. For instance the '620' which only appears for $\delta T \approx -200$ K is mentioned at a depth of 656 km in Table 1 because of its large Clapeyron slope, +0.174 km K^{-1} ('620' $\approx 656 - 0.174 \times 200$ km). For simplicity we mostly discussed our results assuming $\gamma_4 = +3.0$ MPa K^{-1} but as explained in Section 3 we can only derive linear relations between Clapeyron slopes. In the last column of Table 1 we report these relations with respect to γ_4 (the third column is in agreement with the last one when $\gamma_4 = +3$ MPa K^{-1}). Ascribing uncertainties to these slopes is difficult. However from the horizontal sizes of the extrema in Fig. 8 the uncertainties are probably as large as 0.02 km K^{-1} (≈0.7 MPa K^{-1}).

5. Conclusion

In this study, we used the competing actions of temperature and velocities on the apparent topography of TZ discontinuities to quantify their respective effects neglecting the possible presence of compositional variations. The expected anti-correlation of the '410' and '660' is largely hidden by the effects of shallow velocity anomalies and the RMS thermal topographies (5.3 and 4.9 km) are lower than that of the corrections (8.5 km).

We suggest that the Clapeyron slope ratios of the two major interfaces of the TZ can be obtained by minimizing the shallow corrections or by assuming the absence of correlation between these corrections and the TZ temperature. The knowledge of the correlation between the TZ temperature and the shallow corrections derived from tomography may be used to improve this estimate (see Supplement S.1) but the exercise is not easy. This correlation is an important parameter that impacts our ability to measure the exact Clapeyron slopes of the '410' and '660'. By comparison the other sources of uncertainty, *e.g.*, the lateral averaging in the migration process or the assumption that the TZ temperature only varies laterally, seem to be less crucial.

The presence of minor seismic discontinuities has been reported below western US by *e.g.*, Simmons and Gurrola (2000), Song et al. (2004), Vinnik et al. (2010), Eager et al. (2010), Schmandt et al. (2011), and more recently Tauzin et al. (2013). These interfaces are very weak and more visible at low temperatures. Two interfaces seem to correspond to a velocity reduction, two interfaces to a velocity increase. We suggest a new method to construct the phase diagram directly from the seismic observations and, through a Z–Γ transform, we estimate the Clapeyron slopes of the potential minor phase changes.

The sharp reduction of velocity at 350 km depth can hardly be explained in term of a transition toward a higher pressure assemblage as it is associated with a shear-wave velocity drop (∼−30% of the conversion amplitude at the '410'). It has been proposed to mark the onset of a low-velocity layer atop the '410' due to dehydration-induced partial melting (Revenaugh and Sipkin, 1994). We preferentially find this layer in cold environments. It may be induced by water rather released from subduction (Tanner et al., 2012) than released from a passive upwelling from the deeper mantle like in the transition zone water filter model of Bercovici and Karato (2003). We find for this discontinuity a Clapeyron slope $\gamma = +3.2$ MPa K^{-1} close to $\gamma_4 = +2.8$ MPa K^{-1}, which suggests that the two interfaces may be intimately related.

The weak interface at '590' (Tauzin et al., 2013; Eager et al., 2010) does not seem to vary much with temperature, with a small Clapeyron slope of −0.4 MPa K^{-1}. It is also associated with a velocity reduction (−20% of the reflection amplitude at the '410'). Its origin remains mysterious although Shen et al. (2014) suggest that this discontinuity is a global feature associated with delamination and accumulation of oceanic crust at the top of the lower mantle.

The interfaces at 520 and 620 km depth being associated with increases of velocity can be more easily related to pressure-induced phase changes. The '520' is likely associated with the wadsleyite–ringwoodite transformation. Its Clapeyron slope is negative and in agreement with laboratory experiments (Suzuki et al., 2000). This signal is however very weak, only 10% of the conversion amplitude at the '410', and its detection is not very reliable. The wd → rw transition is expected to be broader and with a smaller velocity jump than that of the ol → wd transition so is less likely visible to converted phases (Bina, 2003).

The '620' discontinuity is found above the '660' in the coldest part of the seismic phase diagram. Due to its close proximity to the '660' signal we cannot reliably constrain its Clapeyron slope though it appears positive and greater than that of the '410' in Figs. 7 and 8. Tauzin et al. (2013) tentatively associated this discontinuity with the onset of stability field of akimotoite $MgSiO_3$ below the triple border between Washington, Oregon and Idaho. The presence of akimotoite owing to cold slabs was also suggested by Schmandt (2012) on the basis of a positive v_s gradient above the '660'. The akimotoite is the product of a phase change of majorite in the garnet component occurring for low temperatures at similar pressure ranges as the rw → pv + mw transition (Hirose, 2002; Akaogi et al., 2002; Ishii et al., 2011).

The phase diagrams that we construct from seismic observations assume that the effects of metastability (see *e.g.*, Kirby et al., 1996) or compositional variations (see *e.g.*, Ricard et al., 2005) are negligible. Water, for instance, would promote the uplift of the '410' and the thickening of the TZ (Wood, 1995; Smyth and Jacobsen, 2006) and may bias our temperature estimates. Other factors

have also been suggested to add complexity to the temperature response of the TZ. The Clapeyron slopes γ for any phase transition may vary slightly with pressure and temperature. The '410' broadens at low temperature and eventually bifurcates into two different transitions at lowest temperature when olivine transforms to ringwoodite rather than wadsleyite (Bina, 2003). These complexities do not seem to affect our seismic phase diagram where the '410' transition remains simple (albeit preceded by the sharp '350' velocity reduction at low temperature). The '660' seems to be thicker both at low and high temperature. This behavior is in agreement with experimental phase diagrams (Hirose, 2002; Bina, 2003) where in cold situation the akimotoite phase may form before the ringwoodite while at high temperature the garnet phase transforms after the ringwoodite.

In conclusion, our method for computing the seismic phase diagrams and estimating the Clapeyron slopes through the "Z–γ stacking" approach, is easy to implement. It can be applied at a much larger scale, *e.g.*, on global datasets of P-to-S conversions (Tauzin et al., 2008), or on other global seismic data such as precursors of S waves reflected halfway between sources and receivers. We also plan to develop the same approach in different frequency bands which should help to further refine the gradients of velocities in the TZ and our knowledge of the phase transitions in the mantle.

Acknowledgements

We thank Jean-Philippe Perillat, two anonymous reviewers, and the editor, for the suggestions to improve the method and the manuscript. This work was supported by a Chaire d'Excellence position from CNRS. We thank the IRIS data center for providing seismological data.

Appendix A. Supplementary material

Supplementary material related to this article can be found online at http://dx.doi.org/10.1016/j.epsl.2014.05.039.

References

Akaogi, M., Ito, E., Navrotsky, A., 1989. Olivine-modified spinel–spinel transitions in the system Mg_2SiO_4–Fe_2SiO_4: calorimetric measurements, thermochemical calculation, and geophysical application. J. Geophys. Res. 94.

Akaogi, M., Tanaka, A., Ito, E., 2002. Garnet–ilmenite–perovskite transitions in the system $Mg_4Si_4O_{12}$–$Mg_3Al_2Si_3O_{12}$ at high pressures and high temperatures: phase equilibria, calorimetry and implications for mantle structure. Phys. Earth Planet. Inter. 132, 303–324.

Becker, T., 2011. On recent seismic tomography for the western United States. Geochem. Geophys. Geosyst. 13, 1–11.

Becker, T., Boschi, L., 2002. A comparison of tomographic and geodynamic mantle models. Geochem. Geophys. Geosyst. 3, 1–48.

Bercovici, D., Karato, S., 2003. Whole mantle convection and transition-zone water filter. Nature 425, 39–44.

Bina, C., 2003. Seismological constraints upon mantle composition. In: Carlson, R. (Ed.), Treatise on Geochemistry, vol. 2. Elsevier Science Publishing, pp. 39–59.

Burdick, S., Hilst, R., Vernon, F., Martynov, V., Cox, T., Eakins, J., Karasu, G., Tylell, J., Astiz, J., Pavlis, G., 2010. Model update January 2010: upper mantle heterogeneity beneath North America from traveltime tomography with global and USArray transportable array data. Seismol. Res. Lett. 81, 689–693.

Chevrot, S., Vinnik, L., Montagner, J., 1999. Global-scale analysis of the mantle Pds phases. J. Geophys. Res. 101, 20203–20219.

Deuss, A., 2007. Seismic observations of transition zone discontinuities beneath hotspot locations. In: Foulger, G., Jurdy, D. (Eds.), Plates, Plumes, and Planetary Processes. Geological Society of America.

Dueker, K., Sheehan, A., 1997. Mantle discontinuity structure from mid-point stacks of converted P to S waves across the Yellowstone Hotspot Track. J. Geophys. Res. 102, 8313–8327.

Eager, K., Fouch, M., James, D., 2010. Receiver function imaging of upper mantle complexity beneath the Pacific Northwest, United States. Earth Planet. Sci. Lett. 297, 140–152.

Gu, Y., Dziewonski, A., Agee, C., 1998. Global de-correlation of the topography of transition zone discontinuities. Earth Planet. Sci. Lett. 157, 57–67.

Gu, Y., Dziewonski, A., Ekstrom, G., 2003. Simultaneous inversion for mantle shear velocity and topography of transition zone discontinuities. Geophys. J. Int. 154, 559–583.

Gu, Y., Sacchi, G., 2009. Radon transform methods and their applications in mapping mantle reflectivity structure. Surv. Geophys. 30, 327–354.

Helffrich, G., 2000. Topography of the transition zone seismic discontinuities. Rev. Geophys. 38, 141–158.

Helffrich, G., Bina, C., 1994. Frequency dependence of the visibility and depths of the mantle discontinuities. Geophys. Res. Lett. 21, 2613–2616.

Hirose, K., 2002. Phase transitions in pyrolytic mantle around 670-km depth: implications for upwelling of plumes from the lower mantle. J. Geophys. Res. 107.

Houser, C., Masters, G., Flanagan, M., Shearer, P., 2008. Determination and analysis of long-wavelength transition zone structure using SS precursors. Geophys. J. Int. 174, 178–194.

Houser, C., Quentin, W., 2010. Reconciling Pacific 410 and 660 km discontinuity topography, transition zone shear velocity patterns, and mantle phase transitions. Earth Planet. Sci. Lett. 296, 255–266.

Irifune, T., Kubo, N., Isshiki, M., Yamasaki, Y., 1998. Phase transformations in serpentine and transportation of water into the lower mantle. Geophys. Res. Lett. 25, 203–206.

Ishii, T., Kojitani, H., Akaogi, M., 2011. Post-spinel transitions in pyrolite and Mg_2SiO_4 and akimotoite–perovskite transition in $MgSiO_3$: precise comparison by high-pressure high-temperature experiments with multi-sample cell technique. Earth Planet. Sci. Lett. 309, 185–197.

Ito, E., Akaogi, M., Topor, L., Navrotsky, A., 1990. Negative pressure–temperature slopes for reactions forming $MgSiO_3$ perovskite from calorimetry. Science 249, 1275.

Katsura, T., Yamada, H., Nishikawa, O., Song, M., Kubo, A., Shinmei, T., Yokoshi, S., Aizawa, Y., Yoshino, T., Walter, M., Ito, E., Funakoshi, K., 2004. Olivine–wadsleyite transition in the system $(Mg,Fe)_2SiO_4$. J. Geophys. Res. 109, 1–12.

Katsura, T., Yoneda, A., Yamazaki, D., Yoshino, T., Ito, E., 2010. Adiabatic temperature profile in the mantle. Phys. Earth Planet. Inter. 183, 212–218.

Kennett, B., Engdahl, E., 1991. Travel times for global earthquake location and phase identification. Geophys. J. Int. 105, 429–465.

Kirby, S., Stein, S., Okal, E., Rubie, D., 1996. Metastable mantle phase transformations and deep earthquakes in subducting oceanic lithosphere. Rev. Geophys. 34, 261–306.

Lawrence, J., Shearer, P., 2006. A global study of transition zone thickness using receiver functions. J. Geophys. Res. 111.

Lawrence, J., Shearer, P., 2008. Imaging mantle transition zone thickness with SdS-SS finite-frequency sensitivity kernels. Geophys. J. Int. 174, 143–158.

Lebedev, S., Chevrot, S., van der Hilst, R., 2002. Seismic evidence for olivine phase changes at the 410- and the 660-kilometers discontinuities. Science 296, 1300–1302.

Li, X., Kind, R., Yuan, X., Sobolev, S., Hanka, W., Ramesh, D., Gu, Y., Dziewonski, A., 2003. Seismic observation of narrow plumes in the oceanic upper mantle. Geophys. Res. Lett. 30, 1334.

Litasov, K., Ohtani, E., Sano, A., Suzuki, A., 2005a. Wet subduction versus cold subduction. Geophys. Res. Lett. 32, 1–5.

Litasov, K., Ohtani, E., Sano, A., Suzuki, A., Funakoshi, A., 2005b. In situ X-ray diffraction study of post-spinel transformation in a peridotite mantle: implication for the 660-km discontinuity. Earth Planet. Sci. Lett. 238, 311–328.

Revenaugh, J., Sipkin, S., 1994. Seismic evidence for silicate melt atop the 410-km mantle discontinuity. Nature 369, 474–476.

Ricard, Y., Mattern, E., Matas, J., 2005. Synthetic tomographic images of slabs from mineral physics. In: van der Hilst, R., Bass, J., Matas, J., Trampert, J. (Eds.), Earth's Deep Interior: Structure, Composition, and Evolution, vol. 160. American Geophysical Union, Washington, D.C., pp. 283–300.

Romanowicz, A., Cara, M., 1980. Reconsideration of the relation between S and P station anomalies in North America. Geophys. Res. Lett. 7, 417–420.

Rondenay, S., 2009. Upper mantle imaging with array recordings of converted and scattered teleseismic waves. Surv. Geophys. 30, 377–405.

Rost, S., Thomas, C., 2002. Array seismology: methods and applications. Rev. Geophys. 40, 1–27.

Schmandt, B., 2012. Mantle transition zone shear velocity gradients beneath USArray. Earth Planet. Sci. Lett. 355–356, 119–130.

Schmandt, B., Dueker, K., Hansen, S., Jasbinsek, J., Zhang, Z., 2011. A sporadic low-velocity layer atop the western U.S. mantle transition zone and short-wavelength variations in transition zone discontinuities. Geochem. Geophys. Geosyst. 12, 1–26.

Schmandt, B., Humphreys, E., 2010. Complex subduction and small-scale convection revealed by body-wave tomography of the western United States upper mantle. Earth Planet. Sci. Lett. 297, 435–445.

Shearer, P., 1991. Constraints on upper mantle discontinuities from observations of long-period reflected and converted phases. J. Geophys. Res. 96, 18147–18182.

Shearer, P., 2000. Upper mantle seismic discontinuities. In: Karato, S.-i., et al. (Eds.), Earth's Deep Interior: Mineral Physics and Tomography from the Atomic to the Global Scale. In: Geophys. Monogr. Ser., vol. 117. AGU, Washington, D.C., pp. 115–131.

Shen, X., Yuan, X., Li, X., 2014. A ubiquitous low-velocity layer at the base of the mantle transition zone. Geophys. Res. Lett. 41, 836–842.

Simmons, N.A., Gurrola, H., 2000. Multiple seismic discontinuities near the base of the transition zone in the Earth's mantle. Nature 405, 559–562.
Smyth, J., Jacobsen, S., 2006. Nominally anhydrous minerals and Earth's deep water cycle. In: Jacobsen, S., van der Lee, S. (Eds.), Earth's Deep Water Cycle. In: Geophys. Monogr. Ser., vol. 167. AGU, Washington, D.C., pp. 1–9.
Song, T., Helmberger, D., Grand, S., 2004. Low-velocity zone atop the 410-km seismic discontinuity in the northwestern United States. Nature 427, 530–533.
Stammler, K., Kind, R., 1992. Comment on "Mantle layering from ScS reverberations, 2, the mantle transition zone" by Justin Revenaugh and Thomas H. Jordan. J. Geophys. Res. 97, 17547–17548.
Stixrude, L., Lithgow-Bertelloni, C., 2005. Mineralogy and elasticity of the oceanic upper mantle: origin of the low-velocity zone. J. Geophys. Res. 110.
Suzuki, A., Ohtani, E., Morishima, H., Kubo, T., Kanbe, Y., Kondo, T., Okada, T., Terasaki, H., Kato, T., Kikegawa, T., 2000. In situ determination of the phase boundary between wadsleyite and ringwoodite in Mg_2SiO_4. Geophys. Res. Lett. 27, 803–806.
Tanner, T., Hirschmann, M., Humayun, M., 2012. The effect of H_2O on partial melting of garnet peridotite at 3.5 GPa. Geochem. Geophys. Geosyst. 13, 1–28.
Tauzin, B., Debayle, E., Wittlinger, G., 2008. The mantle transition zone as seen by global Pds phases: no clear evidence for a thin transition zone beneath hotspots. J. Geophys. Res. 113.
Tauzin, B., van der Hilst, R., Wittlinger, G., Ricard, Y., 2013. Multiple transition zone seismic discontinuities and low velocity layers below western United States. J. Geophys. Res. 118, 2307–2322.
Vinnik, L., Ren, Y., Stutzmann, E., Farra, V., Kiselev, S., 2010. Observations of S410p and S350p phases at seismograph stations in California. J. Geophys. Res. 115, 1–12.
Wittlinger, G., Vergne, J., Tapponnier, P., Farra, V., Poupinet, G., Jiang, M., Su, H., Herquel, G., Paul, A., 2004. Teleseismic imaging of subducting lithosphere and Moho offsets beneath western Tibet. Earth Planet. Sci. Lett. 221, 117–130.
Wood, B., 1995. The effect of H_2O on the 410-kilometer seismic discontinuity. Science 268, 74–76.